Harnessing Waves with Folds: A Flexible Origami-inspired Wave Energy Converter

Jingyi Yang[1, 6], Zhong You[1, *], Maozhou Meng[2], Tom Tosdevin[2], Alistair Borthwick[2], John Chaplin[3], Bohan Chen[1], Siming Zheng[4, 2], Martyn Hann[2], Shanshan Cheng[2], Xinyu Wang[2], Krishnendu Puzhukkil[2], Malcolm Cox[5], Kieran Monk[2], Deborah Greaves[2, *]

1. Department of Engineering Science, University of Oxford, Parks Road, Oxford, U.K.
2. School of Engineering, Computing and Mathematics, University of Plymouth, Drake Circus, Plymouth, U.K.
3. Faculty of Engineering and Physical Sciences, University of Southampton, Southampton, U.K.
4. State Key Laboratory of Ocean Sensing & Ocean College, Zhejiang University, Zhoushan, China.
5. Griffon Hoverwork Ltd., Hazel Road, Woolston, Southampton, U.K.
6. Advanced Forming Division, Singapore Institute of Manufacturing Technology, A*STAR, Cleantech Loop, Singapore

* Corresponding authors. Email zhong.you@eng.ox.ac.uk; deborah.greaves@plymouth.ac.uk

Abstract

Ocean waves offer sustainable power yet the design of efficient and durable wave energy converters (WECs) remains challenging. We focus on a WEC that harvests energy from chamber volume change as two bottom-hinged plates open and close with passing wave troughs and crests, driving a turbine generator. For the first time, we present an origami-inspired enclosed WEC whose plates are linked by rigid pleats and confined membrane regions. Unlike traditional flexible WECs that connect the flaps with elastic membranes that stretch, our design achieves predictable cyclic motion through origami folding mechanisms. Using an analytical design method, we optimize dimensions of the pleats and membranes that keep membrane strain minimal during operation. The analytical design is confirmed by finite element analyses, which indicates negligible membrane strain under normal operation, therefore long fatigue life. Tests on a 1:160 scale prototype achieve a capture width ratio of 0.35 and demonstrate robustness under irregular waves and deliberate misalignment. Our WEC design allows the power take-off (PTO) system to be positioned above sea level, ensuring the PTO system operates in air and remains unaffected even if sealing fails. These results demonstrate the potential of origami-inspired WECs as viable and scalable approaches to wave energy harvesting.

Keywords: origami-inspired design, folding-dominate volume change, wave energy converter, small strain.

1. Introduction

Wave energy converters (WECs) extract renewable energy from the ocean and have potential applications that range from powering offshore aquaculture stations to grid-scale electricity generation. Over the past fifty years, various designs have emerged, including attenuators (e.g., Pelamis [1]), point absorbers (e.g., CETO [2, 3], Seabased [4] and CorPower Ocean [5]), oscillating water columns (OWC) (e.g., Wavegen Limpet [6] and Mighty Whale [7]), and overtopping devices (e.g., Wave Dragon [8]). Other notable systems include Oyster [9], WaveRoller [10], and Bombora [11]. While these systems demonstrate the potential to capture wave energy, a persistent issue in submerged or floating WECs concerns their sealing, particularly at interfaces where mechanical motion crosses the boundary between seawater and dry internal chambers. For example, CorPower Ocean, a floating heaving-type point absorber, generates power through a vertical sliding tether that penetrates the sealed power take-off (PTO) chamber of the buoy through a dynamic shaft seal. Although this design permits easy access for inspection and maintenance, the use of a sliding interface introduces long-term reliability concerns: the dynamic seal is vulnerable to fatigue, leading to water ingress and subsequently, increased friction, jamming of the sliding block and PTO failure. The design of WaveRoller avoids this issue by fully enclosing rotational mechanical linkages and PTO components within a sealed base unit. WaveRoller is a seafloor-mounted surge-type WEC with no moving parts crossing the wet-dry boundary. Rotational joints, unlike sliding ones, are more robust under irregular loading and less prone to wear, making them better suited for use in harsh environments. While this design significantly reduces the risk of sealing failure, it sacrifices accessibility for maintenance and repair because the entire system is enclosed and operates below sea level. This prompts the question: can we design a WEC with the PTO positioned above sea level to enhance both accessibility and sealing reliability, while only using rotational joints for simplicity and robustness?

Among the concepts that have been put forward, we build our design on an enclosed V-shaped wedge WEC [12]. This device consists of two rigid flaps connected by a bottom hinge. Preliminary investigations at the COAST Laboratory, University of Plymouth, demonstrated the hydrostatic functionality of this concept [13, 14], but the lack of an enclosed shell resulted in seawater ingress. In the present work, we introduce a design featuring a fully enclosed V-shaped wedge that supports a turbine and PTO mounted above sea level. The design enables air exchange between the internal chamber and the ambient atmosphere, allowing wave-induced pressure variations to drive airflow through the turbine and generate power.

One solution for chamber enclosure is to connect the two flaps with elastic membranes, like a balloon sandwiched between two rigid plates. However, this type of balloon experiences substantial deformation as air is pumped into and out of the chamber. Consequently, a considerable portion of energy is expended on material deformation, thereby reducing the energy available for PTO. Moreover, repeated large deformation of elastic membranes causes material fatigue, compromising long-term reliability.

To overcome these limitations, we propose an origami-inspired WEC design that connects flaps with origami pleats and functions like a bellow [15-18]. This approach reduces strain energy through rigid-foldable mechanisms, enabling folding motion to occur via rotational hinges and preserving the rigidity of panel facets. In practice, rigid bellows cannot be fully enclosed because the bellows conjecture states that enclosed flexible structures cannot change volume without in-plane deformation or self-intersection [19-23]. We therefore use an innovative engineering approach to circumvent this challenge: compliant facets are used to bear localized strain [24-26], with the rigid facets remaining strain-free to provide structural integrity and allow predictable rigid-body motion. We optimize the geometry of the origami-inspired WEC to minimize strain while maximizing volumetric change during the folding process, thereby increasing the energy capture efficiency of the WEC and ensuring its survivability in extreme sea states. The energy-conversion pathway is as follows: incoming waves drive the motion of the bottom-hinged flaps, inducing a change in chamber volume that forces air to flow through a bidirectional air-turbine generator mounted on the top surface of the central frame, which is then converted into useful power. The device can be either moored to the seabed or else integrated with submerged offshore wind turbine foundations.

To test the design concept, we fabricated and tested prototypes of the origami-inspired WEC fixing in heave for different wave conditions, including regular waves and irregular sea states. In the downscaled prototype, we used orifice plates to represent damping of the air-turbine PTO system as is also the practice for OWC-type devices with orifice-loaded chambers [27]. This PTO strategy is compatible with other PTO approaches, such as mechanical direct-drive generators, air springs, dielectric elastomer generators, and direct fluid generators [28-31]. During operation, part of the incident wave energy is used to deform the folding outer shell, while the remainder is available for extraction by the PTO.

The paper is structured from hereon as follows. Section 2 describes the methodology underpinning our origami-inspired bellows-type WEC design through an analytical approach.

The small-strain design is then confirmed through finite element simulations. Section 3 outlines the physical model test facility and instrumentation. Section 4 reports the results obtained for the WEC in regular and irregular sea states, the latter corresponding to a Joint North Sea Wave Project (JONSWAP) spectrum [32] at the Wave Hub test site, Cornwall, UK. Section 5 discusses the advantages, limitations, and practical implementation of the proposed WEC, and closes with the major findings and recommendations.

2 Small-strain origami-inspired WEC

2.1 Design of single origami-inspired bellows section

Figure 1 presents an idealized view of one origami bellows section in (a) fully expanded and (b) partially expanded states. The dotted lines represent valley creases, whereas solid lines are mountain creases. The origami bellows section is not a rigid foldable motion structure according to the bellows conjecture. We therefore release the constraint by using two materials in each section: rigid origami pleats and elastic membranes. The rigid origami pleats are highlighted in blue and function as a rigid-foldable mechanism; the pleats rotate around the creases and drive the opening and closing of the bellows section, transforming it into a motion structure with one degree of freedom (DoF). We define θ_s to be the dihedral angle between two rectangular facets that are connected at the bottom along QP. This angle serves as an input parameter that uniquely determines the folded state of the origami bellows section. In the current design, the range of θ_s is selected to be $0 < \theta_s < \pi/6$. The resulting output angles, φ_t and φ_s, represent the dihedral angles between the two trapezoid top facets and two triangular side facets, respectively, with $0 < \varphi_t, \varphi_s < \pi$. To simplify the design, we set $\varphi_t = \varphi_s$ throughout the full range of motion.

To determine the kinematics of the origami bellows section, we begin by defining three primary parameters: the rectangular facet dimensions w (width) and h (length), and the maximum dihedral angle $\theta_{s,max}$ of the origami section. All other geometric dimensions are derived in relation to these parameters. Specifically, the sector angles are set as

$$\angle AQC = \angle DQC = \frac{\theta_{s,\max}}{2}, \tag{1}$$

ensuring that the dihedral angle φ_s between the side pleats reaches π when the origami is fully expanded (Fig. 1(a)). To synchronize the motion of the top and side pleats, we impose $\varphi_t = \pi$

at the fully expanded state. This can be achieved by specifying the height of the top trapezoids ABFH and DBFE as

$$a = h \cdot \sin(\angle \mathrm{AQC}). \tag{2}$$

In the folding process of the origami section, it is always true that

$$h \cdot \sin(\frac{\theta_s}{2}) = a \cdot \sin(\frac{\varphi_t}{2}) \tag{3}$$

$$\text{and} \qquad \varphi_t = \varphi_s \tag{4}$$

Combining Eqs (1) to (3), we obtain the kinematic relationships

$$\sin(\frac{\theta_s}{2}) = \sin(\frac{\theta_{s,\max}}{2}) \cdot \sin(\frac{\varphi_t}{2}) \text{ and } \varphi_t = \varphi_s \tag{5}$$

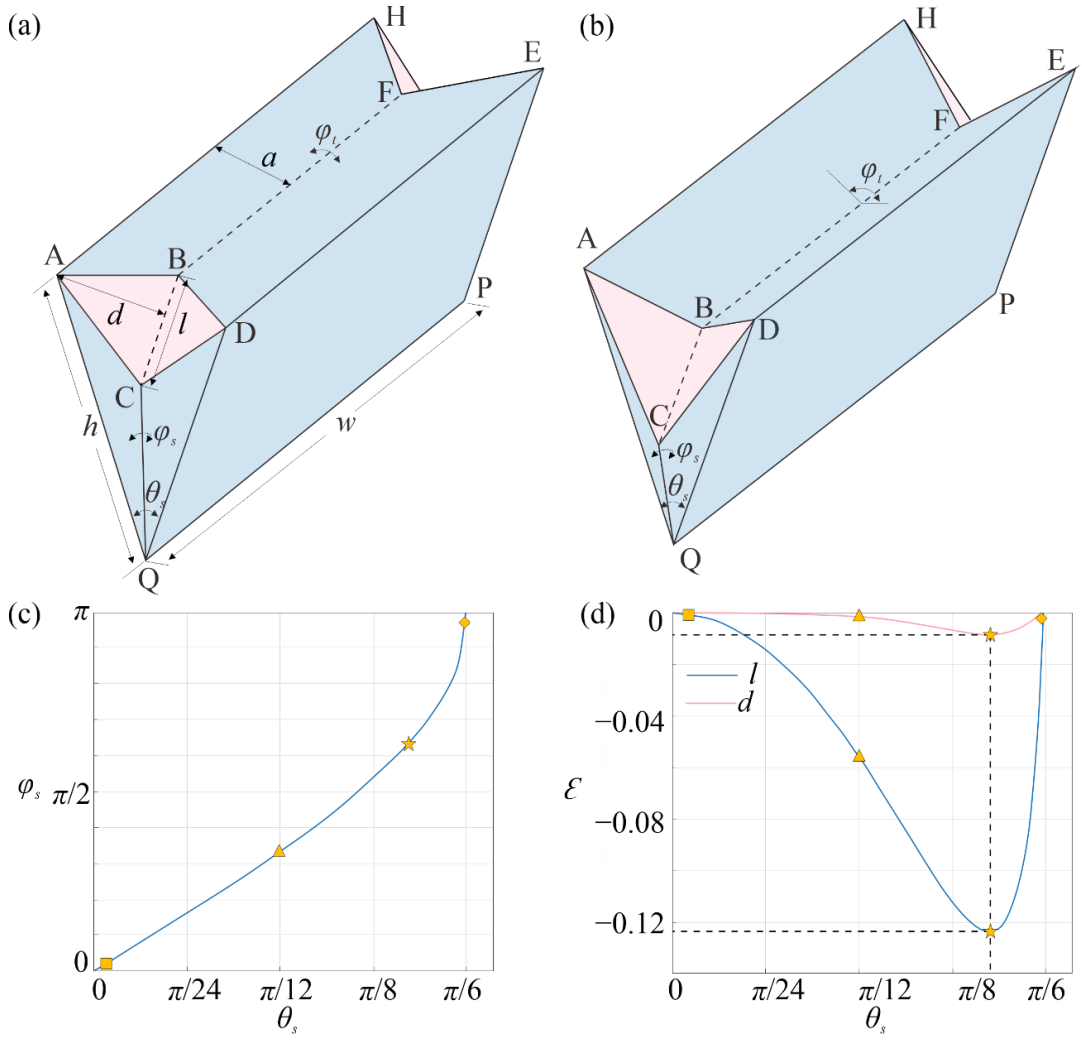

Fig. 1 Small-strain origami-inspired bellow section in (a) fully expanded state, and (b) a partially folded state. Rigid facets are in blue whereas elastic membranes are in red. The dotted lines denote valley creases, and solid lines are mountain creases. (c) Kinematic relationship of the rigid-foldable origami skeleton. (d) Membrane strain along two orthogonal directions during the folding process.

Figure 1(c) depicts the resulting kinematic relationships between θ_s and φ_s. When $\theta_s = \pi/6$, both the top pleats and side pleats are completely extended, i.e., $\varphi_t = \varphi_s = \pi$, giving the fully expanded state shown in Fig. 1(a). Decreasing θ_s causes φ_t and φ_s to decrease until all dihedral angles are zero, in which case the origami bellow section is folded flat. To ensure complete enclosure, the rigid origami pleats are connected using elastic membranes, highlighted in red. During the motion cycle, the rigid facets undergo rigid body rotation about the creases, governing the overall motion and preserving structural integrity while constraining deformation to the elastic membranes. Noting that elastic membranes only resist tensile load and become slack under compression, we design the origami geometry so that the membranes remain slack throughout the full range of motion, thereby avoiding any stress accumulation. It is achieved by the compressive strain along two orthogonal dimensions of the membrane, l and d. Appendix A gives a brief description of the algorithm developed to optimise the geometry. The optimization process is carried out iteratively using the Matlab *fmincon* function with an interior-reflective Newton approach [33], continuing until a local minimum is found. Figure 1(d) shows the membrane strain for the optimized origami section, which experiences zero strain at either fully folded state ($\theta_s = 0$) or fully expanded state ($\theta_s = \pi/6$). Otherwise, the strains along the l and d directions are negative, indicating the membrane is slack. Consequently, the origami bellow experiences zero strain throughout the motion. Four states are highlighted with different markers in Fig. 1(c), corresponding to the same markers in Fig. 1(d), respectively.

2.2 Finite element model of an origami bellow section

Note that the optimized geometry of the origami structure is derived geometrically without considering material thickness. To validate the design, finite element analysis (FEA) is conducted using Abaqus software [34] with optimized dimensions of the origami plates and elastic membranes as input. Due to symmetry, one half of the origami bellows section is considered in the simulation (Fig. 2(a)). Points M, N, and K are introduced to define the line of symmetry of trapezoids ABFH and DBFE. A Cartesian coordinate system O-xyz is established with the origin O at the midpoint of edge QP. The y-axis is aligned with edge QP, the z-axis points from O to N, and the x-axis obtained by the right-hand rule. We apply symmetric boundary condition on edges MN, KN, OK, and OM. Nodal coordinates are stored in an input file for meshing. The triangular membrane surfaces, ΔABC and ΔDBC are represented by 3-noded linear membrane elements (M3D3). The nodes along their shared

interface are tied using the built-in function in Abaqus, ensuring that both surfaces move as a single, unified unit. The origami pleats, ΔDCQ and ΔACQ, are represented by 3-noded linear shell elements with reduced integration (S3R). The rectangular origami skeleton, AMOQ and DKOQ, and trapezoids, AMNB and DKNB, are represented by 4-noded linear shell elements with reduced integration (S4R). The region-of-interest membrane, ΔABC and ΔDBC, is simulated using an elastic-perfectly plastic constitutive model with von Mises failure criterion, whereas the remaining surfaces are modelled as steel plates. The membrane used in the simulation is high-density polyethylene, whose material properties are as follows: material density of 950 kg/m^3, Young's modulus of 1.1 GPa, yield strength (ultimate tensile stress) of 33 MPa, and Poisson's ratio of 0.42 [35].

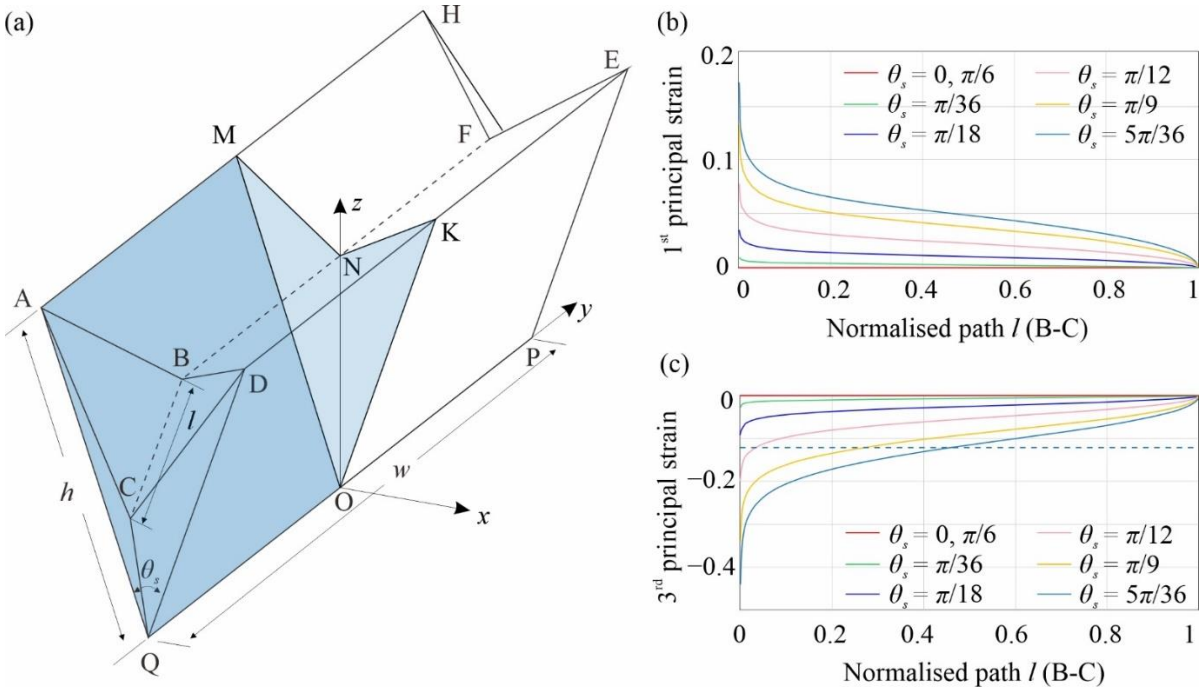

Fig. 2 FEA of an origami bellows section. (a) The model (highlighted in blue). (b-c) Distribution of the first and the third principal strains along path *l* during folding process.

The strain along path *l* was extracted for analysis, noting that the strain along the orthogonal path *d* is negligible. Figures 2 (b-c) show the first and third principal strains along path *l* at representative dihedral angles θ_s of the origami section, corresponding to orthotropic strains under tension and compression, respectively. The principal strains increase as the origami section expands, reaching maximum values when $\theta_s = 5\pi/36$, then decay to zero when $\theta_s = \pi/6$.

Notably, the third principal strain exhibits higher absolute values than the first principal strain, indicating that the mechanical behavior of the membrane is primarily governed by compressive deformation, which is physically in slack. When $\theta_s = 5\pi/36$, the average third principal strain reaches 0.129, as shown by the dotted line in Fig. 2(c), comparable to the theoretical prediction in Fig. 1(d). Despite the overall compressive dominance, the finite element simulations reveal localized tensile stress concentrations at point B. To address this, a high-elongation silicone adhesive was used to bond the membrane to the rigid pleats when fabricating the physical prototype.

2.3 Volumetric change of a single origami bellows section

We then calculate the volumetric change of one optimized bellows section when it is in motion. The V-shaped wedge is decomposed into three parts as shown in Fig. 3(a). The volume V_s is approximated by subtracting the volume of a truncated triangular prism V_2 from that of a large triangular prism V_1 and then adding the volume of four identical tetrahedra V_3. The triangular prism V_1 has a base ΔADQ and a height of w. The surface area of ΔADQ is calculated as

$$S_{\Delta ADQ} = \frac{1}{2} \cdot AD \cdot (h \cdot \cos\frac{\theta_s}{2}) = \frac{1}{2} \cdot (2h \cdot \sin\frac{\theta_s}{2}) \cdot (h \cdot \cos\frac{\theta_s}{2}) \tag{6}$$

Its volume is

$$V_1 = \frac{1}{2} \cdot (2h \cdot \sin\frac{\theta_s}{2}) \cdot (h \cdot \cos\frac{\theta_s}{2}) \cdot w \tag{7}$$

The truncated triangular prism V_2 is approximated as a full triangular prism of base ΔADB' and height w, without considering truncation. This approximation is justified because the length of BF exceeds 92% of DH and AE. Before truncation, the surface area of the triangular base is

$$S_{\Delta ADB'} = \frac{1}{2} AD \cdot (a \cdot \cos\frac{\varphi_t}{2}) = \frac{1}{2} \cdot (2h \cdot \sin\frac{\theta_s}{2}) \cdot (a \cdot \cos\frac{\varphi_t}{2}) \tag{8}$$

Its volume is thus approximated to be

$$V_2 = \frac{1}{2} \cdot (2h \cdot \sin\frac{\theta_s}{2}) \cdot (a \cdot \cos\frac{\varphi_t}{2}) \cdot w \tag{9}$$

The tetrahedron is approximated as having a triangular base ΔCQB' whose surface area is

$$S_{\Delta CQB'} = \frac{1}{2} QB' \cdot CG = \frac{1}{2} \cdot (h \cdot \cos\frac{\theta_s}{2} - a \cdot \cos\frac{\varphi_t}{2}) \cdot (QC \cdot \sin\beta), \tag{10}$$

where β is the angle between B'Q and CQ. Eq. (10) can be solved with the four special vectors $\overrightarrow{CG}$, $\overrightarrow{GQ}$, $\overrightarrow{QA}$, and $\overrightarrow{AC}$ forming a loop. The pyramid has a height equal to the perpendicular distance from the base to the vertex A, i.e., $h \cdot \sin\frac{\theta_s}{2}$. The volume of one tetrahedron is

$$V_3 = \frac{1}{3} S_{\Delta CQB'} \cdot (h \cdot \sin\frac{\theta_s}{2}). \tag{11}$$

Having obtained the volume of each component, the volume of one origami section is approximately

$$V_s = V_1 - V_2 + 4 \cdot V_3. \tag{12}$$

By combining Eqs. (3), (4), and (6)-(12), the volume of a single origami section can be approximated as a function of its opening angle θ_s. Fig. 3(b) shows this relationship, below which photographs are presented of the downscaled physical prototype and its configuration at selected θ_s values. The near-linear relationship between the volume ratio V_s/V_{s0} (where V_{s0} is the volume of the fully expanded origami section) and θ_s indicates that the volumetric change of an origami bellows section depends primarily on the magnitude of the angular change $\Delta\theta_s$, rather than the initial opening angle.

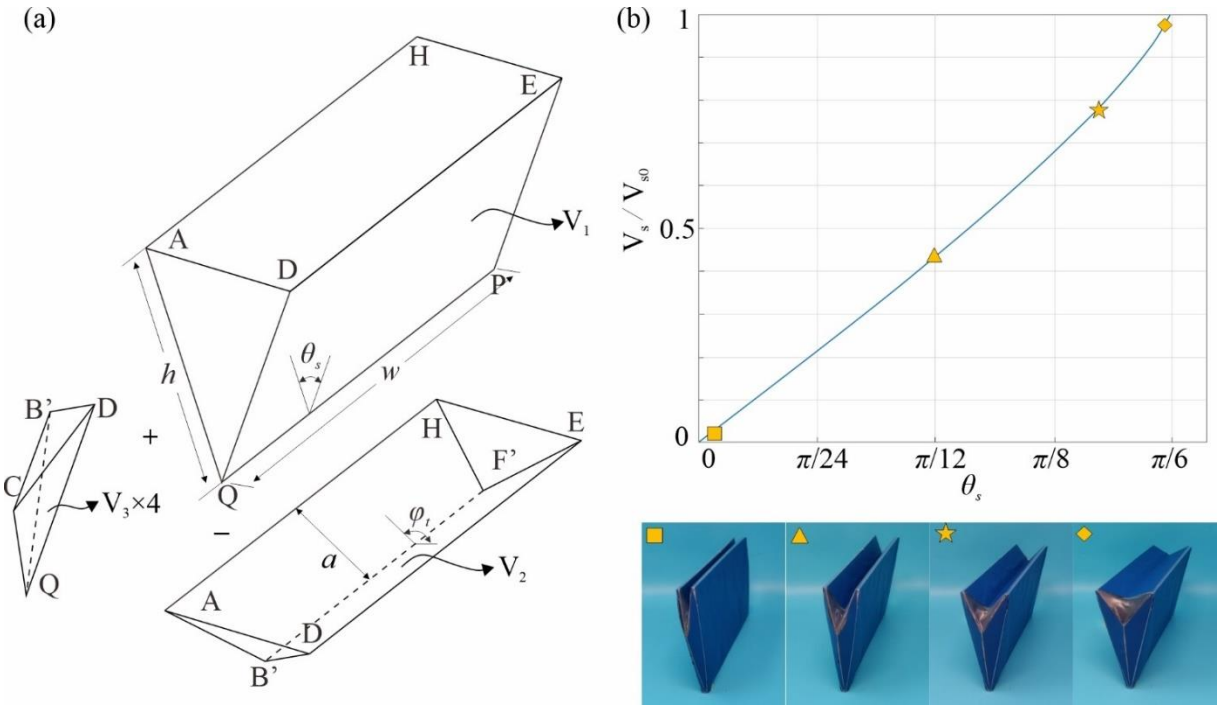

Fig. 3 (a) Single origami section decomposed into three components; the volume is calculated by subtracting V_2 from V_1 and adding $4V_3$. (b) Normalized volume of a single origami section as a function of section angle θ_s.

2.4 Design and volumetric change of multiple-section WEC

A WEC is formed by arranging multiple identical origami sections side-by-side. For example, Fig. 4(a) has two sections that are positioned symmetrically on either side of a central rigid frame, each supported by internal structures (shaded in grey in the cross-sectional view). A ballast cylinder is mounted beneath the central frame by supporting bars and moored to the seabed to maintain the orientation of the WEC and ensure its upright stability.

Oriented perpendicular to incoming waves, the WEC has two flaps: an upwave flap (which is the first to encounter the wave front) and a downwave flap. The flaps are allowed to rotate about hinges located along the bottom of the central frame. We name this rotation 'flap motion' and characterize it by the opening angles of the upwave flap and downwave flap, denoted θ_u and θ_d, respectively. As a wave crest passes, a larger portion of the WEC becomes submerged, increasing the hydrostatic force and causing the flaps to close, thus reducing their opening angles. Conversely, as a wave trough passes, the submersion decreases, and the opening angle of the flaps increases. This continuous change in submersion drives variations in θ_u and θ_d, enabling air intake and expulsion through a turbine generator PTO system mounted on the top of the central frame, enabling power generation.

Linear torsion springs are placed at the bottom hinges to counteract hydrostatic load on the flaps; these springs are pre-stressed when the flaps are extended out and provide increasing torque as the flaps fold inwards. Depending on the relationship between wavelength and WEC geometry, the upwave flap may encounter a wave crest at the same instant the downwave flap encounters a trough. In such situations, the flaps move independently.

The power generation depends on air exchange between the WEC chamber and the ambient environment. The chamber volume of the WEC comprises a volume contributed by the central frame V_c, the volume of the downwave side V_d, and upwave side V_u. It is expressed as

$$V = V_c + V_d + V_u. \tag{13}$$

The volume of the central frame is given by $V_c = h \cdot w \cdot w_c$, where h and w are the length and width shared with the flap dimensions, and w_c is the third side length of the rectangular prism. To calculate the varying components V_d and V_u, we assume that the two origami sections on each side of the WEC evenly divide the flap angles, such that $\theta_d = 2\theta_{s,d}$ and $\theta_u = 2\theta_{s,u}$, where $\theta_{s,d}$ and $\theta_{s,u}$ are the dihedral angles of one origami section on the downwave side and upwave side of the WEC, respectively. Once the dihedral angles $\theta_{s,d}$ and $\theta_{s,u}$ have been determined, the

corresponding volume of the origami sections, $V_{s,d}$ and $V_{s,u}$, is then obtained. The volumes of the downwave and upwave sides are expressed as $V_d = 2V_{s,d}$, and $V_u = 2V_{s,u}$.

Figure 4(b) presents a surface plot of the chamber volume of the WEC as a function of θ_u and θ_d, with snapshots of the physical model representing the numbered corners on the plot. The volume undergoes smooth changes, except when θ_u or θ_d equals 0 or $\pi/6$, which correspond to the four cornered configurations.

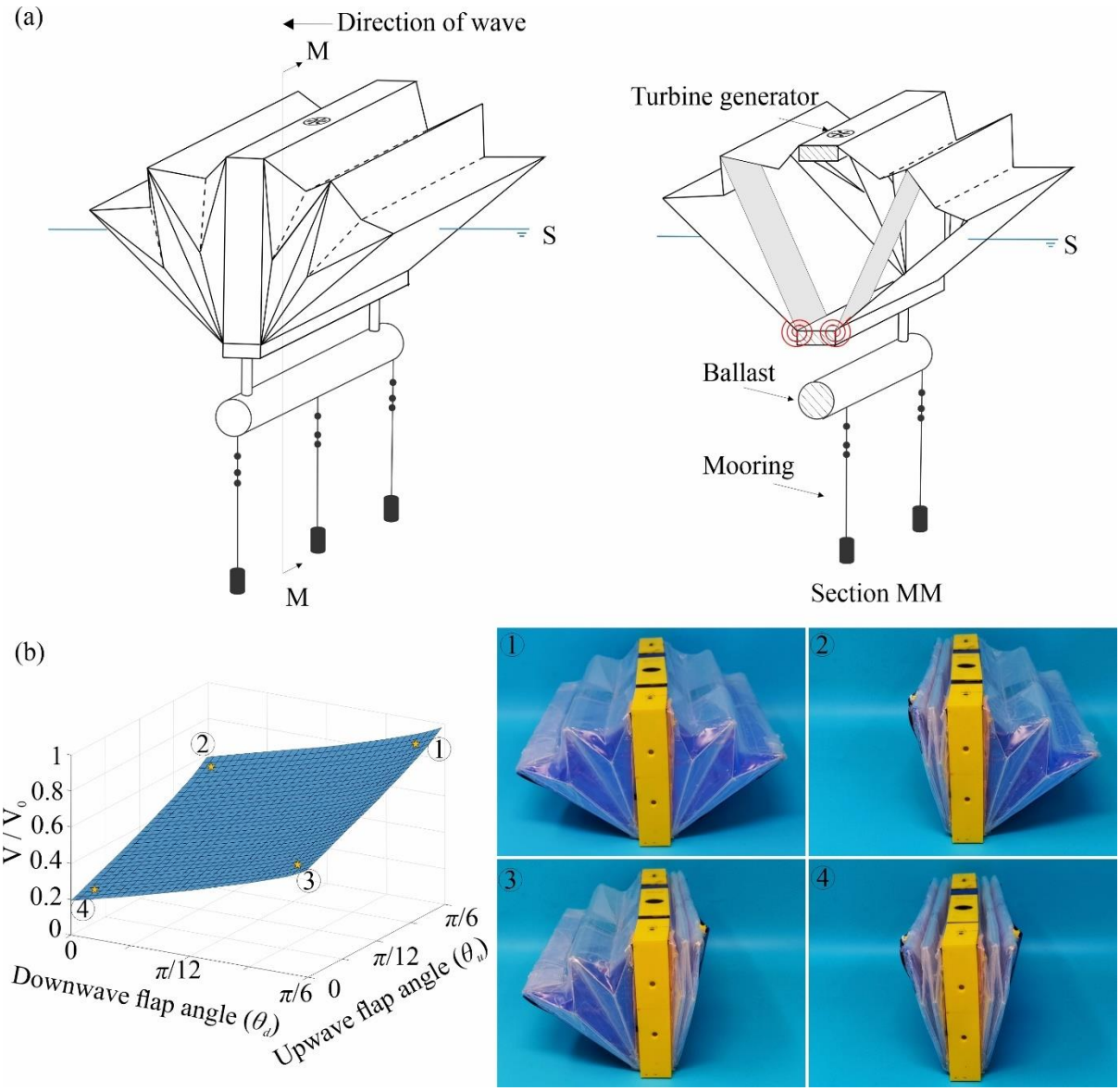

Fig. 4 WEC Design. (a) Isometric and cross-sectional views of the WEC. (b) Normalized chamber volume as a function of downwave and upwave flap angles, with photographs showing corresponding configurations of the downscaled physical prototype.

3 Physical model for coastal-basin tests

3.1 Physical model of origami-inspired WEC

A 1:160 physical model was fabricated and tested to assess the energy absorption performance of the WEC. The methodology followed Froude scaling laws, and effectively preserves dynamic similarity, but neglects viscous and surface tension effects. In constructing the model, the top surfaces of the panels were connected for valley creases, whereas the bottom surfaces were hinged for mountain creases. The 1:160 downscaled prototype was constructed with flap dimensions of 250 mm × 129 mm using 1 mm thick acrylic boards for the pleats and internal supporting structures and 2.5 mm thick acrylic boards for the flaps and central frames. The foldable skeleton was encapsulated in 0.12 mm thick polyethylene film (Fig. 4(b) and Fig. 5). Other key dimensions of the prototype are listed in Table 1.

Table 1. Detailed geometry of origami-inspired WEC with Froude scaling multiplier $\lambda = 160$.

Parameter	Symbol	Scale factor	Model value	Full-scale value
length	PQ (w)	λ^1	250 mm	40.00 m
	AQ (h)	λ^1	129 mm	20.65 m
	BF	λ^1	0.92w	36.80 m
	CQ	λ^1	0.69h	14.24 m
	AB	λ^1	0.27h	5.57 m
	AC	λ^1	0.38h	7.84 m
angle	$\theta_{s,\,max}$	1	$\pi/6$	$\pi/6$
	∠AQC	1	$\pi/12$	$\pi/12$

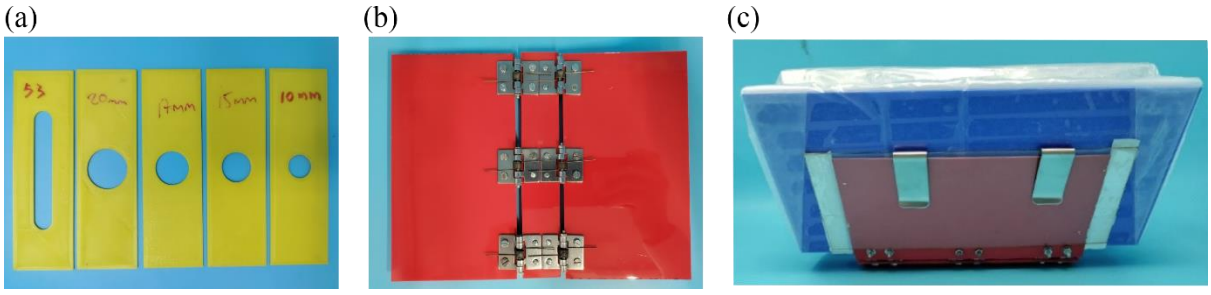

Fig. 5 Downscaled physical model with replaceable orifice plates and torsional spring fixture. (a) Orifice plates. (b) Torsional stiffness fixture. (c) Stiffness plate inserted and clipped into a frame holder on the exterior wall of the flaps.

We used interchangeable orifice plates to impose controlled damping for the turbine generator and PTO system. Each plate was mounted on top of the central frame to regulate air exchange between the WEC chamber and the ambient atmosphere. Orifice plates were fabricated from PLA material using additive manufacturing techniques. The designs included a slot orifice of 10 mm width, 53 mm length, and two half-circle ends, and circular orifices of 20 mm, 17 mm, 15 mm, and 10 mm diameter (Fig. 5(a)). By selecting the orifice plate geometry, the air exchange rate and damping was adjusted for different test conditions.

Furthermore, the hinge of each flap had adjustable torsional spring stiffness (Fig. 5(b)). The stiffness fixture facilitated three configurations by means of replaceable linear torsional springs. Each hinge consisted of three 1.5 mm thick polycarbonate plates connected by linear torsional springs on both sides. The springs were at their natural lengths when the stiffness plate is flat. The middle plate matched the width of the central frame of the downscaled physical prototype. When inserted into the frame holder attached to the external walls of the flaps (Fig. 5(c)), the springs were strained, generating torque that acted along the flap hinges. Linear torsional springs used in the tests were sourced from McMaster-Carr®. For the low-stiffness configuration, the fixture was used without any torsional springs. For the mid-stiffness configuration, three 180° left-hand wound linear springs of stiffness 0.26 N·mm/° (item number 9271K94) were installed along each hinge. For the high-stiffness configuration, three 180° left-hand wound linear springs of stiffness 0.35 N·mm/° (item number 9271K98) were used along each hinge.

3.2 Coastal-basin experimental setup

Under normal sea states, the flaps oscillate about an equilibrium position to generate power, whereas in extreme weather such as storms or tsunamis, both flaps can be folded inward (configuration ④ in Fig. 4(b)) to enhance survivability.

To understand how the origami-inspired enclosed WEC design performs under wave loading, the 1:160 downscaled physical prototype was tested in the coastal basin at the University of Plymouth. The basin measured 15.5 m in length, 10 m in width, and had an operating depth of 0.5 m (Fig. 6). The physical prototype was fixed in heave at various drafts (0.465h, 0.527h, 0.543h, and 0.567h), permitting only flap motions and synchronised pleat motions. An increased draft reduces the equilibrium flap angle of the WEC in still water due to greater

hydrostatic force. The prototype was positioned 4.315 m from the wave makers, centred along the width of the coastal basin. A wave probe was placed 0.5 m lateral to the prototype to monitor the real-time wave amplitude experienced by the device. The flap motion of the model WEC was tracked using a Qualisys motion capture system®, with four motion cameras placed along the side of the basin to monitor markers attached to each flap and the fixed frame. A pressure sensor [36] mounted on the central frame measured the differential pressure across the orifice. Both the motion capture and pressure measurements were synchronized through LabView software [37], with data recorded at a sampling rate of 128 Hz.

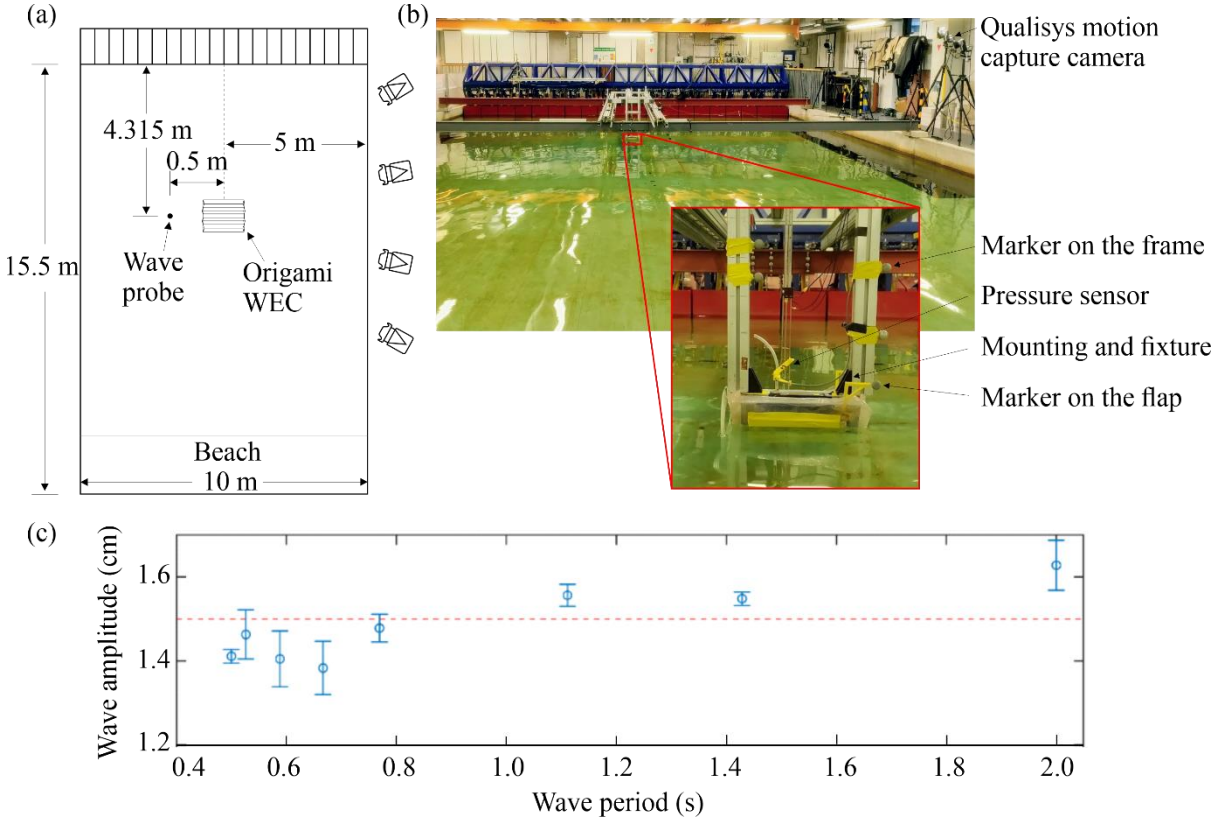

Fig. 6 Tests on a downscaled model at fixed draft in the COAST Laboratory, University of Plymouth, UK: (a) plan view of the setup; and (b) photographs of the model in coastal basin. (c) Measured mean wave amplitudes with standard deviations in the Coastal Basin, University of Plymouth. The wave maker target was 1.5 cm amplitude for periods 0.5–2 s (dotted line). Circles denote means, whereas error bars denote standard deviations.

The prototype was first tested in regular incident waves of amplitude 1.5 cm and periods ranging from 0.5 s to 2 s, corresponding to full-scale waves of amplitude 2.4 m and periods between 6.32 s and 25.3 s. To ensure reliability of the test results, the repeatability of the waves generated in the basin was assessed. For each wave condition, five empty basin tests were

performed with the WEC removed from the water and replaced by a wave probe positioned at the WEC location. The wave maker paddles operated for 60 s during each run, and the true wave amplitudes were recorded by the probe. For each test, data sampled during the final five wave cycles were analyzed, and corrections applied to account for wave reflection from the beach. Mean values of wave amplitude and standard deviation were calculated for each regular wave period considered (Fig. 6(c)).

3.3 Key performance metrics in a representative test run

A representative test was conducted with the physical model configured at 0.567h draft, equipped with a 53 mm slot orifice, and fitted with highest torsional spring stiffness along the hinges, for a wave period of 0.588 s. Figures 7(a)-(c) present time histories of the measured pressure drop across the orifice, the flap angle, and the volumetric flow rate through the WEC chamber for five consecutive wave cycles. Three metrics are used to assess the performance of the WEC as defined below.

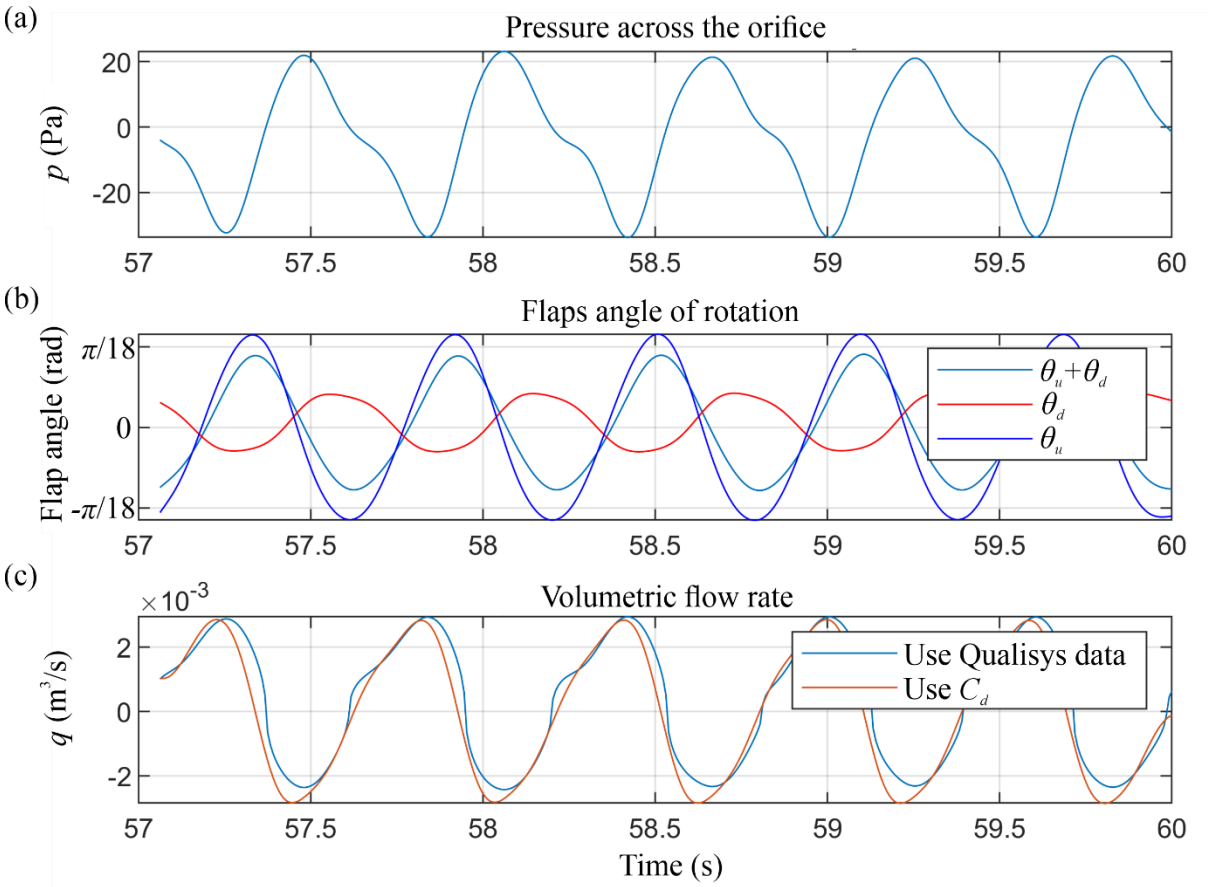

Fig. 7 Measured time histories of (a) pressure drop, (b) flap angles, and (c) volumetric flow rate of air for the test achieving highest CWR.

The first metric is the mean value of the peak to trough pressure drop computed over the five wave periods (see Fig. 7(a)).

The second metric is the response amplitude operator for flap rotation (RAO_θ) defined as the ratio of the mean flap rotation amplitude to the incident wave amplitude. RAO_θ was determined by first computing the mean wave amplitude over five wave periods from gauge data obtained using the empty basin. Corresponding Qualisys data for the WEC that captured the rotational motion of the upwave and downwave flaps were obtained over the same five wave periods (Fig. 7(b)). The instantaneous total flap angle was given by

$$\theta_{\mathrm{WEC}} = \theta_u + \theta_d. \tag{64}$$

It was assumed that the two origami sections each side of the WEC evenly divided the flap angles, such that $\theta_d = 2\theta_{s,d}$ and $\theta_u = 2\theta_{s,u}$, where $\theta_{s,d}$ and $\theta_{s,u}$ are the dihedral angles of one origami section on the downwave side and upwave side of the WEC, respectively. The maximum change in θ_{WEC} was then calculated for each wave period, and the mean value over five periods was taken to be the final RAO_θ value.

The third key performance indicator is the Capture Width Ratio (CWR), which describes the proportion of power absorbed by the WEC relative to the total incident wave power traveling through the WEC chamber, and is defined as

$$\mathrm{CWR} = \frac{P_o}{P_w \cdot w_e} \tag{15}$$

where P_0 is the time average absorbed power by the WEC, P_w is the time average incident wave power, and w_e is the effective width of the WEC chamber.

The absorbed power by the WEC P_0 is determined through averaging over several whole wave periods as

$$P_0 = \frac{1}{T_s}\int_0^{T_s} | \, p(t) \cdot q(t) \, | dt \tag{16}$$

where $p(t)$ is the pressure drop across the orifice, $q(t)$ is the volumetric flow rate of the air passing through the orifice, and T_s is the averaging time span (typically a multiple of the wave period). The volumetric flow rate $q(t)$ of air passing through the WEC orifice was derived from the flap motions θ_u and θ_d using two approaches. In the first approach, the WEC chamber volume was determined using the relationship shown in Fig. 4(b), and $q(t)$ obtained by differentiation. The second approach relied upon the orifice discharge equation

$$q(t) = A_0 C_d \sqrt{\frac{2|p(t)|}{\rho_a}}, \tag{17}$$

where A_0 is the cross-sectional area of the orifice, C_d is the orifice discharge coefficient, and ρ_a is air density. On rearranging Eq. (17), a mean value of orifice discharge coefficient was determined for the exhalation and inhalation cycles through the orifice, using $q(t)$ obtained from the first method and the measured $p(t)$. The resulting C_d value was then applied to calculate $q(t)$ from Eq. (17) for the given wave conditions and WEC setup for the same orifice. Figure 7(c) compares the time histories of the volumetric flow rate of air through the orifice over about five wave periods: the two calculation approaches give similar results.

Incident wave power P_w for each condition was estimated using linear wave theory (Appendix B); the results are summarized in Table 2. The mean amplitudes and standard deviations are taken from the empty-basin measurements in Fig. 6(c).

Table 2. Incident wave conditions tested in empty basin.

Water depth D (cm)	Wave period T (s)	Measured mean amplitude a (cm)	Amplitude Standard deviation σ (cm)	Wavelength L (cm)	Relative depth D/L	Water depth	Steepness a/L	Wave power P_w (W/m)	Max wave power (W/m)	Min wave power (W/m)
50	2	1.63	0.060	405.64	0.123	Intermediate	0.004	2.23	2.39	2.07
50	1.428	1.55	0.016	264.45	0.189	Intermediate	0.006	1.57	1.61	1.54
50	1.111	1.56	0.026	181.11	0.276	Intermediate	0.009	1.18	1.22	1.14
50	0.769	1.48	0.033	92.18	0.542	Deep	0.016	0.65	0.68	0.62
50	0.667	1.38	0.064	69.38	0.721	Deep	0.020	0.49	0.54	0.45
50	0.588	1.40	0.067	54.02	0.926	Deep	0.026	0.44	0.48	0.40
50	0.526	1.46	0.059	43.25	1.156	Deep	0.034	0.43	0.47	0.40
50	0.5	1.41	0.017	39.03	1.281	Deep	0.036	0.38	0.39	0.37

4 Results

4.1 WEC performance in regular waves

Figure 8 summarizes the dynamic performance of the prototype for various drafts, torsional spring stiffnesses, and orifice dimensions in terms of the key performance metrics: p_{max}, RAO_θ, and CWR. Here, p_{max} and RAO_θ were obtained from the measured data, whereas CWR was calculated using Eqs. (15)-(17) with mean values of incident wave power P_w as listed in Table 2.

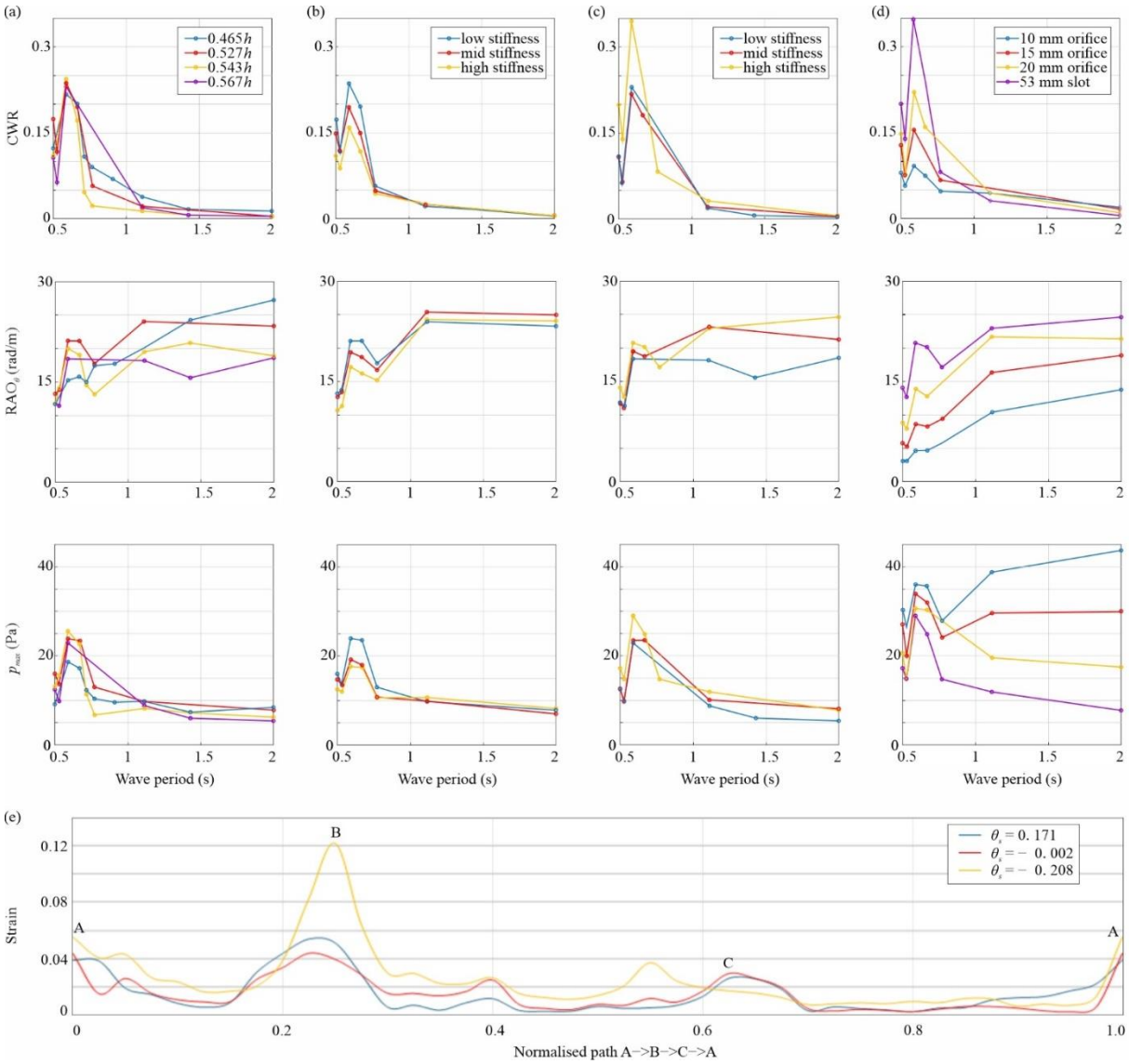

Fig. 8 WEC performance under regular wave conditions. CWR, RAO$_\theta$, and maximum differential pressure p_{max} of the 1:160 downscaled prototype with (a) 53 mm slot orifice, the lowest stiffness, and different drafts; (b) 53 mm slot orifice, 0.527h draft, and various stiffness values; (c) 53 mm slot orifice, 0.567h draft, and various stiffness; (d) 0.567h draft, highest stiffness, and various orifice dimensions; and (e) distribution of the first principal strain along path ABCA from simulation.

Across the range of wave periods tested, the CWR consistently peaked at a wave period of 0.588 s (equivalent to 7.44 s wave for the scaled-up model). The highest CWR of 0.35 was achieved with the prototype model set at a draft of 0.567h, the highest torsional stiffness configuration at each hinge, and a 53 mm slot orifice for air exchange. Supplementary Video V1 provides a video recording of this test run. Under these conditions, asymmetric flap motions were observed, attributed to the short wavelength of 54 cm (27 cm between a wave crest and

trough) relative to the prototype dimensions. This caused one flap to align with the wave crest while the other was positioned in the trough, resulting in unsynchronized motions. More symmetric flap motions were observed using the same setup during a test run with waves of longer wavelength (181.11 cm, corresponding to 1.11 s wave period), as shown in Supplementary Video V2.

Interestingly, increasing the draft alone did not significantly enhance the CWR within the test range (Fig. 8(a)). Although draft adjustments influenced the equilibrium angles of the WEC, these changes did not result in substantial improvement in energy absorption efficiency. However, the effect of torsional spring stiffness on CWR depended strongly on the draft. At a smaller draft of 0.527h, increasing the torsional stiffness reduced the CWR (Fig. 8(b)). This reduction was primarily due to energy dissipation during deformation of the torsional springs. Conversely, at a larger draft of 0.567h, increased stiffness improved the CWR (Fig. 8(c)). This occurred because the larger draft resulted in smaller equilibrium flap angles. Addition of torsional springs increased these angles, enhancing the flap motion and enabling more efficient energy capture. Comparing the two yellow curves representing high-stiffness hinges at different drafts in Fig. 8(b) and Fig. 8(c), both RAO_θ and the maximum pressure drop across the orifice p_{max} increase with a larger draft, leading to a higher CWR (Video recordings of the WEC with different drafts are provided in Supplementary Video V3).

Orifice dimensions significantly influenced the performance of the WEC. The largest orifice, offering minimal resistance to airflow, yielded the highest RAO_θ for the flaps. However, this reduced resistance also led to a smaller pressure differential across the orifice. Despite this, the largest orifice achieved the highest CWR at a wave period of 0.588 s but exhibited a narrower bandwidth across the range of wave periods considered (Fig. 8(d)). This highlights the trade-off between pressure drop and volumetric flow rate when optimizing WEC performance through orifice selection.

We further assessed fatigue under the wave condition that produced the highest CWR (test run in Fig. 7). The time-dependent differential pressures across the orifice, measured at different flap angles, were applied to the membrane surface at element nodes. Transient stresses at representative flap angles were then computed with the Abaqus Dynamic/Explicit solver. Figure 8(e) shows the first principal strain along path A → B → C → A for three representative dihedral angles of an origami section under wave loading. Using the worst-case nodal stress from the dynamic analysis, we performed fatigue evaluation in FE-Safe [38]. The stress was

cycled from −1 to +1 in normalised amplitude, and life was computed with the Goodman criterion [39] using the S–N for the polyethylene material used in the downscaled model [40]. FE-Safe mitigated the influence of mesh driven stress concentrations that can increase with finer discretisation. Under the examined operating condition, the membrane is predicted to endure loading up to the maximum cycles specified in the fatigue curve (690,000 cycles).

4.2 WEC performance for various orientations and in irregular waves

The performance of the WEC was evaluated at 0, $\pi/6$ and $\pi/2$ orientations (Fig. 9(a)) relative to the wave front, with 0.567h draft, mid torsional hinge stiffness, and 15 mm circular orifice. Three performance metrics, i.e., the maximum differential pressure p_{max}, absorbed power P_0, and CWR, were assessed for the WEC in regular waves of amplitude 1.5 cm and wave period ranging from 0.5 s to 2 s (Fig. 9(b)). Supplementary Videos V4 and V5 show the responses of the WEC under various orientations for wave periods of 0.588 s and 1.111 s.

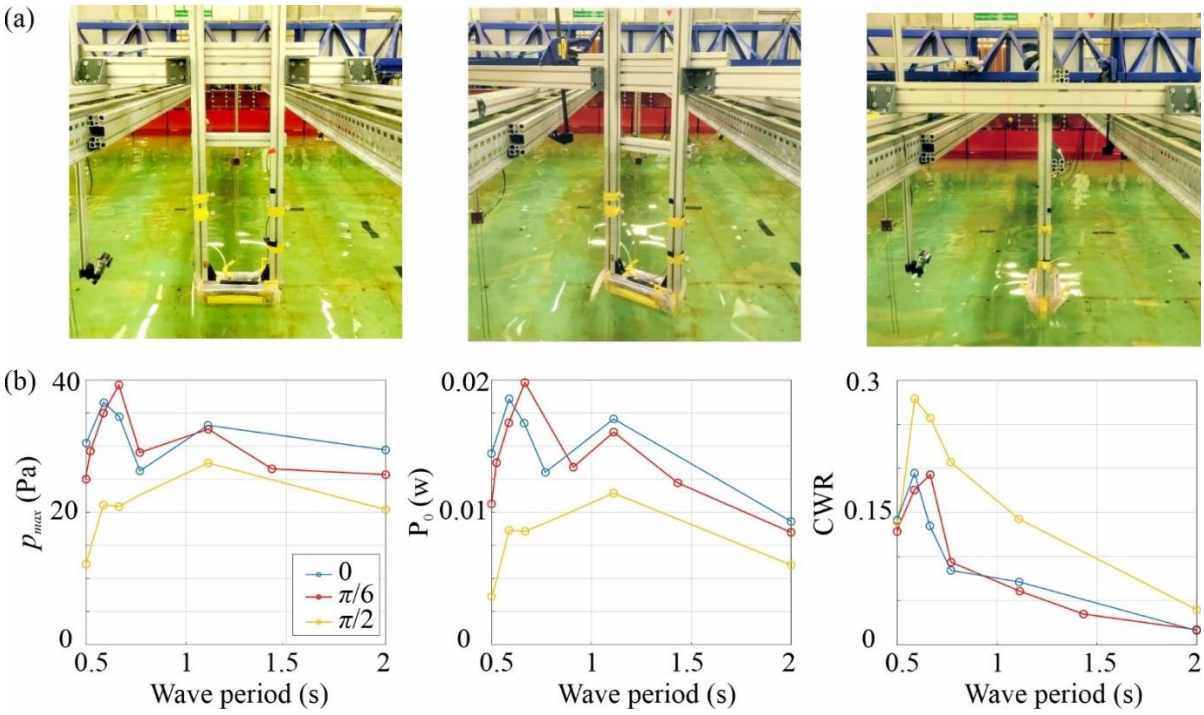

Fig. 9 (a) Physical prototype placed at different orientations relative to the incident wave direction in the coastal basin. Left to right: 0, $\pi/6$ and, $\pi/2$ radians with respect to the wave front. (b) WEC performance at different orientations to the wave front.

The WEC in $\pi/6$ orientation attained broader bandwidth performance without compromising peak P_0 and CWR; this confirmed the robustness of the WEC design under angled misalignments. For $\pi/2$ orientation, the differential pressure and absorbed power were lower, but higher values of CWR were achieved due to the reduced wave-facing width w_e. Furthermore, the WEC exhibited more synchronized flap motions in waves of shorter wavelength due to symmetric wave loading on the two flaps caused by alignment of the incident wave direction with the central axis of the device. Flap motion tracking at the $\pi/2$ orientation was not feasible with the Qualisys system due to the camera's view of the reflective markers being obscured by the device. Instead, the volumetric flow rate was calculated using the discharge coefficient C_d and differential pressure $p(t)$, using Eqn. (17).

Next, the 1:160 downscaled prototype was tested under irregular wave conditions (Fig. 10(a)), replicating those at the Wave Hub site off the north coast of Cornwall, UK. The tests simulated mean wave conditions with a significant wave height (H_s) of 2 m, a peak wave period (T_p) of 9.8 s, and a peak distribution factor (γ) of 3.3. For the downscaled prototype, this corresponded to a significant wave height of 1.25 cm and a peak wave period of 0.775 s in the coastal basin. Each test ran for 4 min 45 s, equivalent to 1 hour of wave activity for the scaled-up model. The prototype was set at a draft of 0.567h and tested for various orifice dimensions and spring stiffnesses. The scaled-up WEC is predicted to produce absorbed power of 60 kW under the prescribed irregular wave conditions (Fig. 10(d)). Smaller orifices (10 mm and 15 mm) achieved higher power absorption, particularly for mid-stiffness, because sufficient differential pressure was maintained across the orifice and losses reduced from deformation of the torsional springs. However, at this small scale, friction suppressed the response to wave action except at larger wave heights. Larger-scale tests are necessary to assess and reduce frictional losses.

In addition to replicating representative irregular waves from the Wave Hub site, we generated irregular wave conditions with peak periods of 8 s and 12 s, while not varying other parameters. The corresponding wave profiles are shown in Figs. 10(b) and (c). Using the optimal setup, the model was further tested under various orientations and irregular waves with different peak periods. The results are presented in Fig. 10(e). Shorter peak wave periods (T_p = 8 s) generally resulted in higher absorbed power, in accordance with regular wave tests and confirming the effectiveness of the WEC when subject to higher-frequency wave states. The WEC with $\pi/6$ orientation maintained a strong performance, demonstrating its robustness to misalignment. The performance reduced for the $\pi/2$ orientation because of the smaller wave-facing width and

less efficient wave interaction. Despite this, the WEC still absorbed 40 kW, demonstrating its ability to operate effectively even for less favorable configurations. Supplementary Video V6 presents the test run recordings replicating the Wave Hub spectrum for the three orientations.

The test cases for irregular waves and various WEC orientations are detailed in Appendix C.

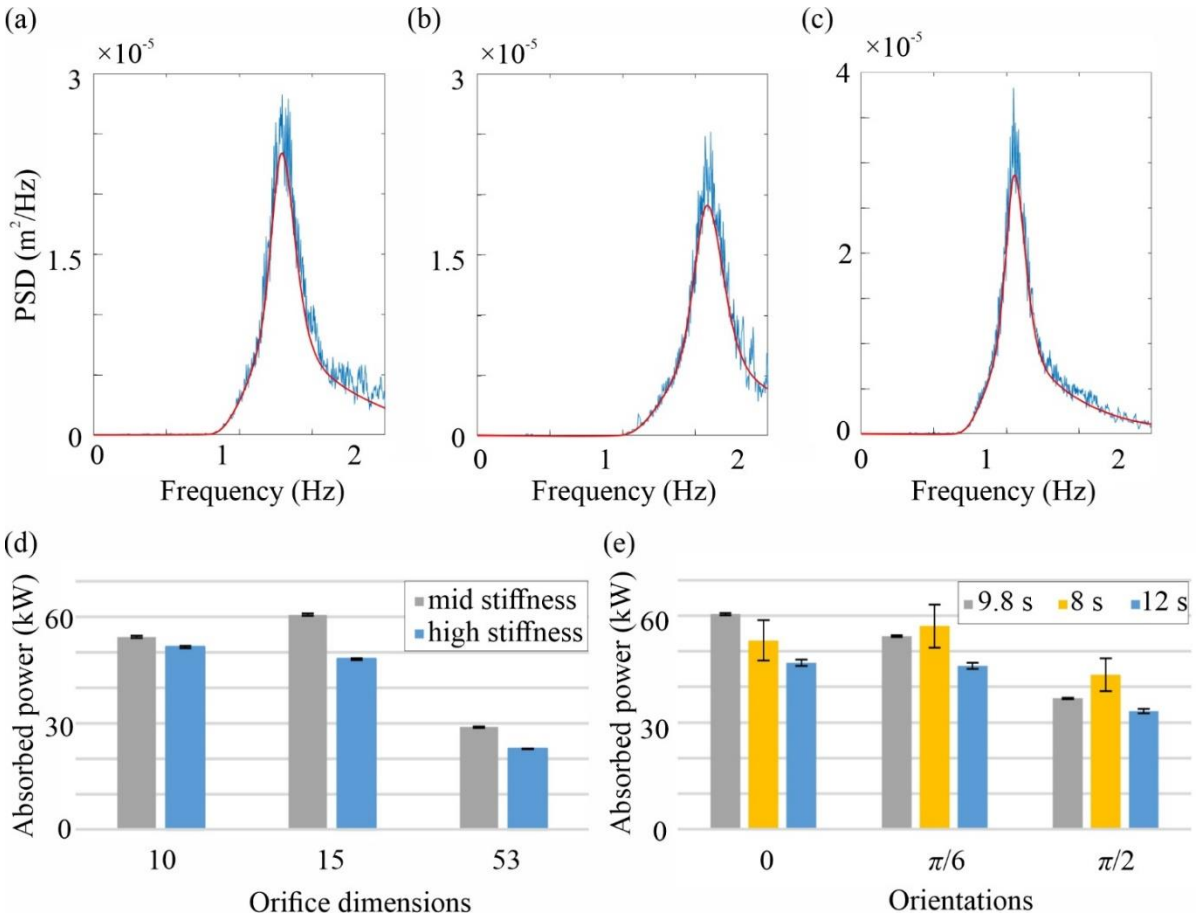

Fig. 10 Scaled irregular wave tests. Free surface elevation spectra for (a) H_s = 2 m, T_p = 9.8 s, error = 0.54%, replicating conditions at the Wave Hub site; (b) H_s = 2 m, T_p = 8 s, error =10.64%; and (c) H_s = 2 m, T_p = 12 s, error: 1.87%. Red curves correspond to expected wave profiles and blue curves to measured wave probe data from empty basin tests. (d) Histograms of absorbed power for the scaled-up model in irregular sea states replicating those at the Wave Hub site, for different values of hinge stiffness and orifice dimension, and (e) various orientations to irregular waves at different peak wave periods.

5 Discussion and conclusions

In this study, we presented an origami-inspired enclosed WEC that inflates under wave troughs and deflates under wave crests, capturing energy via a turbine generator. Unlike conventional inflatable designs that rely on material stretching, our WEC achieves volumetric change

through rigid-panel folding to provide predictable cyclic motions. The geometry of the WEC was optimized to ensure that the structure undergoes minimal deformation when operating, and we confirmed this through finite element analysis. Our small-strain design should reduce internal energy losses, thereby improving the efficiency of wave energy conversion by allowing a greater portion of incident wave energy to be absorbed. It also enables the WEC to have a prolonged fatigue life.

A 1:160 downscaled prototype was fabricated and tested. Under regular waves, a peak CWR of 0.35 was observed for wave amplitude of 2.4 m and period of 7.44 s. The energy-absorbance performance of the WEC is related to a combination of parameters including draft, stiffness, and damping of the model. The prototype also demonstrated robustness under irregular wave conditions and varying orientations relative to the incident wave direction. A scaled-up model, based on one-hour equivalent sea states replicated from the Wave Hub site, is projected to generate up to 60 kW of power. Remarkably, the WEC maintained high energy absorption even when misaligned by up to $\pi/3$ from the wave direction, indicating low sensitivity to orientation. This directional robustness broadens the range of viable deployment scenarios, including applications where precise alignment is not feasible.

Furthermore, the WEC design places the PTO system above sea level, so that it interacts solely with air. This arrangement eliminates failure modes associated with seawater ingress even if sealing is compromised, addressing a longstanding challenge affecting submerged or floating WECs where dynamic seals often become failure points.

The origami-inspired WEC design offers a fresh perspective on WEC design. The concept suits nearshore sites with seabed moorings as well as integration with submerged offshore wind turbine foundations, particularly those with equilateral layouts where WEC units can be installed along each side. The compact-foldable design of the origami-inspired WEC also has potential as a power source for self-sustaining marine robots and sea-state monitoring probes.

The limitations of the present work should motivate future design studies. The highest CWR obtained is modest and rather narrow banded, but could potentially be doubled by introducing a tuned added-mass system [41]; for example, auxiliary water-filled bodies that increase the effective inertia of the flaps could be attached to the origami WEC. Further improvements in wave energy capture may be achieved by adjusting flap hinge stiffness and mooring configuration across different sea states, thus altering the dynamic response and resonant

period. Minimization of friction effects within the system should also improve the performance of origami-inspired WECs. Friction effects are particularly dominant in small-scale tests and may significantly affect the performance achieved in experiments, this could be investigated through testing larger-scale models. Finer resolution for wave periods near resonance is necessary for a more comprehensive understanding of the wave energy capture efficiency of the WEC. Such advancements will further enhance the performance and scalability of this origami-inspired WEC, supporting its broader adoption in renewable energy applications.

Acknowledgements

The authors would like to thank Mr. Francis Rebbeck for his valuable assistance in setting up the experimental tank. We also acknowledge the support of the EPSRC grant EP/V040227/1.

References

[1] Henderson, R. (2006). Design, simulation, and testing of a novel hydraulic power take-off system for the Pelamis wave energy converter. *Renewable energy*, 31(2), 271-283.

[2] Faizal, M., Ahmed, M. R., & Lee, Y. H. (2014). A design outline for floating point absorber wave energy converters. *Advances in Mechanical Engineering*, 6, 846097.

[3] Zhu, K., Greaves, D., Shi, H., Wei, Z., Wang, T., Lu, Q., ... & Cao, F. (2026). A comparative study on the dynamic performance of floating and submerged wave energy converter arrays. *Ocean Engineering*, *343*, 123461.

[4] Chatzigiannakou, M.A.; Dolguntseva, I.; Ekström, R.L.; Leijon, M. Offshore Deployment of Marine Substation in the Lysekil Research Site. In Proceedings of the 25th International Ocean and Polar Engineering Conference (ISOPE 2015), Kona, Big Island, HI, USA, 21–26 June 2015.

[5] Todalshaug, J. H., Ásgeirsson, G. S., Hjálmarsson, E., Maillet, J., Möller, P., Pires, P., ... & Lopes, M. (2016). Tank testing of an inherently phase-controlled wave energy converter. *International Journal of Marine Energy*, *15*, 68-84.

[6] Lynn PA (2013). *Electricity from wave and tide: an introduction to marine energy*, 1st edn. Wiley, Chichester, 199–202.

[7] Falcão, A. F. & Henriques, J. C. (2016). Oscillating-water-column wave energy converters and air turbines: A review. *Renewable energy*, *85*, 1391-1424.

[8] Kofoed, J. P., Frigaard, P., Friis-Madsen, E., & Sørensen, H. C. (2006). Prototype testing of the wave energy converter wave dragon. *Renewable energy*, *31*(2), 181-189.

[9] Whittaker, T., Collier, D., Folley, M., Osterried, M., Henry, A., & Crowley, M. (2007, September). The development of Oyster—a shallow water surging wave energy converter. In *Proceedings of the 7th European wave and tidal energy conference* (pp. 11-14).

[10] Apolonia, M., & Simas, T. (2021). Life cycle assessment of an oscillating wave surge energy converter. *Journal of Marine Science and Engineering*, *9*(2), 206.

[11] Algie, C., Ryan, S., & Fleming, A. (2017). Predicted power performance of a submerged membrane pressure-differential wave energy converter. *International journal of marine energy*, 20, 125-134.

[12] Farley, F. J. M. (2012). Free floating bellows wave energy converter. *UK Patent GB2488185*.

[13] Phillips, J. W. (2017). *Mathematical and Physical Modelling of a Floating Clam-type Wave Energy Converter* (Doctoral dissertation, University of Plymouth).

[14] Zheng, S., Phillips, J. W., Hann, M., & Greaves, D. (2023). Mathematical modelling of a floating Clam-type wave energy converter. *Renewable Energy*, *210*, 280-294.

[15] Guest, S. D. & Pellegrino, S. (1994). The folding of triangulated cylinders, part II: the folding process.

[16] Hoberman, C. (2007). Collapsible containers. *United States Patent Application Pub. No. 2007/0007289 A1*.

[17] Yoshimura, Y. (1955). "On the mechanism of buckling of a circular cylindrical shell under axial compression".

[18] Miura, K. & Tachi, T. (2010). "Synthesis of rigid-foldable cylindrical polyhedra," *Symmetry: Art and Science,* pp. 204-213.

[19] Connelly, R., Sabitov, I., & Walz, A. (1997). The bellows conjecture. Beitr. *Algebra Geom*, 38(1), 1-10.

[20] Connelly, R. (1977). A counterexample to the rigidity conjecture for polyhedra. *Publications Mathématiques de l'IHÉS*, 47, 333-338.

[21] Connelly, R. (1978). A flexible sphere. *The Mathematical Intelligencer*, *1*, 130-131.

[22] Bricard, R. (1897). Mémoire sur la théorie de l'octaèdre articulé. *Journal de Mathématiques pures et appliquées*, 3, 113-148.

[23] Tachi, T. (2017). Capping rigid origami tubes. In *Proceedings of IASS Annual Symposia* (Vol. 2017, No. 13, pp. 1-10). International Association for Shell and Spatial Structures (IASS).

[24] Yang, J., You, Z., Cheng, S., Wang, X., Puzhukkil, K., Cox, M., ... & Greaves, D. (2023). Origami-adapted clam design for wave energy conversion. In *Proceedings of the European Wave and Tidal Energy (EWTEC) Conference* (Vol. 15). DOI: 10.36688/ewtec-2023-329.

[25] Zeng, F., Wang, T., & Li, J. (2025). Origami-inspired dual-mode wave energy harvesting for ocean buoys. *Energy*, *320*, 135131.

[26] Greaves, D., Tosdevin, T., Borthwick, A., Yang, J., You, Z., Meng, M., ... & Chaplin, J. (2025, September). Flexible Responsive Systems in Wave Energy. In *Proceedings of the European Wave and Tidal Energy Conference* (Vol. 16). DOI: 10.36688/ewtec-2025-1237.

[27] Raghavan, V., Simonetti, I., Metrikine, A. V., Lavidas, G., & Cappietti, L. (2024). A new numerical modelling framework for fixed oscillating water column wave energy conversion device combining BEM and CFD methods: Validation with experiments. *Ocean Engineering*, *301*, 117543.

[28] Zakaria, M. F. U. A. P. (2025). State of the art of Power Take Off (PTO) systems in Wave Energy Converter (WEC). *Ocean Engineering*, *335*, 121669.

[29] Caselli, M., Carloni, A., Cherubini, A., Moretti, G., Fontana, M., & Vertechy, R. (2025). Submerged Stadium-Shaped Pressure Differential Dielectric Elastomer Generator for Wave Energy Conversion. *IEEE Access*, *13*, 197912-197925.

[30] Gurjar, K. V. S., Sadangi, A. S., Kumar, A., Ahmad, D., Patra, K., Collins, I., ... & Zweiri, Y. (2025). Dielectric elastomer generators: recent advances in materials, electronic circuits, and prototype developments. *Advanced Energy and Sustainability Research*, *6*(1), 2400221.

[31] Huang, Y., Xiao, Q., Idarraga, G., Yang, L., Dai, S., Abad, F., ... & Lotfian, S. (2025). Bio-inspired adaptive flexible tube wave energy converters: Resonant fluid–structure interaction and power extraction. *Physics of Fluids*, *37*(5).

[32] Hasselmann, K., Barnett, T. P., Bouws, E., Carlson, H., Cartwright, D. E., Enke, K., ... & Walden, H. (1973). Measurements of wind-wave growth and swell decay during the Joint North Sea Wave Project (JONSWAP). *Ergaenzungsheft zur Deutschen Hydrographischen Zeitschrift, Reihe A.*

[33] Coleman, T.F., Li, Y. (1994), On the convergence of interior-reflective Newton methods for nonlinear minimization subject to bounds, *Math. Program*. 67, 189–224.

[34] Smith, M. (2009). *ABAQUS/Standard User's Manual, Version 6.9*. Dassault Systèmes Simulia Corp.

[35] Ashby, M. (2016). Material property data for engineering materials. *Engineering Department and Granta Design*, 27.

[36] Honeywell pressure sensor. Manufacturing number HSCSAAN010NDAA5. Retrieved from https://www.mouser.com/datasheet/2/187/HWSC_S_A0012826924_1-3073319.pdf

[37] National Instruments. (2024). *LabVIEW 2023 SP1* [Computer software]. Austin, TX: National Instruments. Retrieved from https://www.ni.com/en-us/shop/labview.html

[38] Dassault Systèmes. (2023). *FE-SAFE (Version 2023)*. Dassault Systèmes Simulia Corp. https://www.3ds.com/products-services/simulia/products/fe-safe/

[39] Goodman, J., *Mechanics Applied to Engineering*, Longman, Green & Company, London, 1899.

[40] Njim, E.K., Bakhy, S.H. and Al-Waily, M., 2021. A study on the influence of stress ratio and loading mode on fatigue life characteristics of porous functionally graded polymeric materials. *International Journal of Energy and Environment*, 12(2), pp.115-12.

[41] Li, X., Martin, D., Jiang, B., Chen, S., Thiagarajan, K., Parker, R. G., & Zuo, L. (2021). Analysis and wave tank verification of the performance of point absorber WECs with different configurations. *IET Renewable Power Generation*, *15*(14), 3309-3318.